

Realizing Stable Relaxor Antiferroelectric and Superior Energy Storage Properties in $(\text{Na}_{1-x/2}\text{La}_{x/2})(\text{Nb}_{1-x}\text{Ti}_x)\text{O}_3$ Lead-Free Ceramics through A/B-Site Complex Substitution

Jun Chen, He Qi, and Ruzhong Zuo*

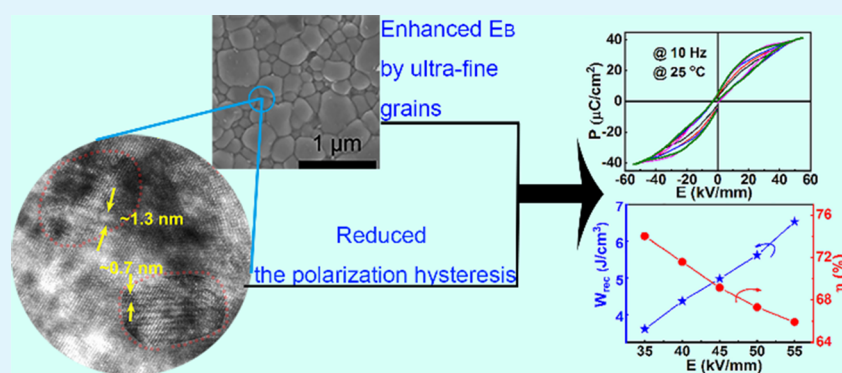
Cite This: *ACS Appl. Mater. Interfaces* 2020, 12, 32871–32879

Read Online

ACCESS |

Metrics & More

Article Recommendations



ABSTRACT: The development of environmentally friendly energy storage dielectrics with high energy storage density has attracted increasing attention in power electronics. The combination of antiferroelectric ceramics with relaxor characteristics proves to be an efficient way to greatly improve energy storage properties. In this work, a novel $(\text{Na}_{1-x/2}\text{La}_{x/2})(\text{Nb}_{1-x}\text{Ti}_x)\text{O}_3$ lead-free bulk ceramic exhibits excellent energy storage properties of a giant recoverable energy storage density $W_{\text{rec}} \approx 6.5 \text{ J/cm}^3$, a relatively high efficiency $\eta \approx 66\%$, and an ultrafast discharge speed $t_{0.9} \approx 50 \text{ ns}$ at $x = 0.18$, showing outstanding potential for pulsed power capacitors. The Rietveld structural refinement and Raman spectra suggest a relaxor antiferroelectric orthorhombic R phase at room temperature as $x > 0.16$. Obviously enhanced breakdown strength can be ascribed to ultrafine grains of $\sim 0.21 \mu\text{m}$ and largely improved resistivity after $\text{BaCu}(\text{B}_2\text{O}_5)$ doping. The detailed analysis of high-resolution transmission electron microscopy and in situ field Raman spectra clearly discloses the existence and rapid response feature of antipolar nanoregions and the resulting high driving field ($\sim 30 \text{ kV/mm}$) for the antiferroelectric-to-ferroelectric phase transition, laying a solid foundation for the achievement of desirable energy storage characteristics. These results would provide a reliable strategy and a good understanding for designing new energy storage capacitor dielectrics.

KEYWORDS: energy storage, lead free, relaxor antiferroelectric, NaNbO_3 , breakdown strength

I. INTRODUCTION

Dielectric capacitors are expected to be used in advanced pulse systems, such as power distribution, transportation devices, and medical devices, due to their high power density and fast charge and discharge rate.^{1,2} Ceramic dielectrics with good mechanical properties, thermal and chemical stability, and fatigue resistance have been widely used in industry.^{3–5} For dielectric capacitors during one electric cycle, the total energy density ($W = \int_0^{P_{\text{max}}} E dP$), recoverable energy density ($W_{\text{rec}} = \int_{P_r}^{P_{\text{max}}} E dP$), and energy storage efficiency ($\eta = \frac{W_{\text{rec}}}{W}$) are the main parameters, where P_{max} is the maximum polarization and P_r is the remanent polarization. The relatively low W_{rec} as one of the main drawbacks for most of ceramic dielectrics limits the lightweight feature and miniaturization of electronic devices, so

it is necessary to develop ceramic capacitors with high energy storage density.^{3,5–9}

Up to now antiferroelectric (AFE) ceramics have been widely reported to exhibit good energy storage properties due to their relatively large ΔP values ($\Delta P = P_{\text{max}} - P_r$), mainly including PbZrO_3 -based,^{10–12} AgNbO_3 -based,^{13–15} and $(\text{Bi}_{0.5}\text{Na}_{0.5})\text{TiO}_3$ -based^{5,16,17} material systems. However, ex-

Received: May 30, 2020

Accepted: July 2, 2020

Published: July 2, 2020



tremely large polarization hysteresis during the first-order AFE–ferroelectric (FE) phase transition usually accompanies significant energy loss, which not only leads to the reduction of W_{rec} and η values but also results in an increase in heat loss, making the materials easier to be disrupted in service.^{2,10–15} Moreover, the large polarization current during the AFE-to-FE phase transition would also increase the probability of the ceramic being electrically broken.

NaNbO_3 (NN) has an AFE structure over a very wide temperature range and shows a P–R phase transition (AFE P: orthorhombic $Pbma$ space group; AFE R: orthorhombic $Pnma$ space group) at $T_{\text{P-R}} \approx 360$ °C on heating.^{18,19} Owing to field-induced irreversible AFE–FE phase transition, poor energy storage properties are usually obtained in pure NN ceramics, as indicated in Figure 1a. After the substitution of some ABO₃

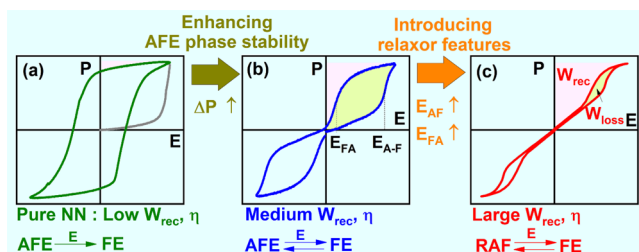


Figure 1. Sketch of the evolution of P – E loops and energy storage properties with enhancing the AFE phase stability and introducing relaxor features in NN-based ceramics: (a) pure NN, (b) enhancing the AFE phase stability, and (c) introducing relaxor features.

perovskites, the stabilized AFE P phase accompanies the achievement of repeatable double P – E loops, leading to gradually optimized energy storage properties, as indicated in Figure 1b.^{20–22} However, large polarization hysteresis can still be found in NN-based ceramics with an AFE P phase. A slim double-like P – E loop with relatively high driving field (E_{AF})

for AFE-to-FE phase transition, low polarization hysteresis, and sluggish phase switching process can be also obtained in relaxor AFE (RAF) ceramics (Figure 1c),^{22–27} as usually observed in relaxor FEs.^{3,28–30}

$(\text{Na},\text{M})(\text{Nb},\text{Ti})\text{O}_3$ is a typical lead-free relaxor system with compositional disorder at both A and B sites, where the valence of M can be +2 or +3.^{22,24,31–33} However, the local symmetry of $(\text{Na},\text{M})(\text{Nb},\text{Ti})\text{O}_3$ ceramics is strongly dependent on the kind and amount of M ions. An RFE phase with tetragonal symmetry can be achieved when M is Ba,³¹ while a stabilized AFE phase has been found when M is Ca, Sr, and Bi.^{22,24,32,33} The formation of the AFE phase in NN originates from the displacement of both A- and B-site cations as well as oxygen octahedral tilting.³⁴ Ba²⁺ with larger radii and smaller electronegativity (Ba²⁺: 1.61 Å and 0.89 Å³; Na⁺: 1.39 Å and 0.93 Å³)³⁵ would tend to inhibit oxygen octahedral tilting and A-site displacement, while the effect of Ca²⁺ (1.34 Å and 1 Å³), Sr²⁺ (1.44 Å and 0.95 Å³), and Bi³⁺ (1.36 Å and 2.02 Å³) is opposite. In addition to the stabilization of AFE phases, the substitution of trivalent ions in NN should effectively enhance the dielectric relaxor behavior compared with that of most of divalent ions. The end member of $(\text{Na}_{1-x}\text{M}^{3+}_{x/2})$ – $(\text{Nb}_{1-x}\text{Ti}_x)\text{O}_3$ ($x = 1$) corresponds to a rhombohedral $R\bar{3}c$ perovskite structure with antiphase octahedral tilting ($(\text{La}_{0.5}\text{Na}_{0.5}\text{TiO}_3)$, where M³⁺ is La³⁺ (1.36 Å and 1.1 Å³).³⁶ It is expected that the AFE phase in NN can be stabilized after complex substitution of La³⁺ and Ti⁴⁺ together with enhanced dielectric relaxor characteristics. In combination with the optimization of dielectric breakdown strength (E_{B}) through further adding sintering aids, a giant $W_{\text{rec}} \approx 6.53$ J/cm³, a desirable $\eta \approx 66\%$, and an ultrafast discharge speed of $t_{0.9} \approx 50$ ns can be achieved, showing attractive prospects for practical applications in advanced pulse systems.

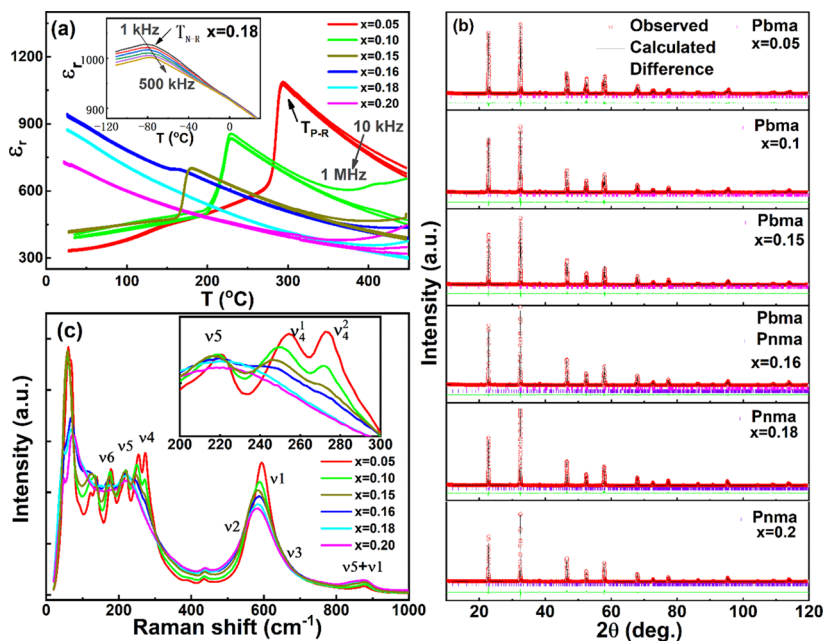


Figure 2. (a) Dielectric permittivity as a function of temperature at 10 kHz–1 MHz for NLNT_x ceramics. (b) Rietveld refinement of conventional XRD. (c) Raman spectra of NLNT_x ceramics. The inset of (a) shows the low-temperature dielectric permittivity of NLNT_{0.18} ceramics. The inset of (c) shows the local amplification of Raman spectra in a range of 200–300 cm^{−1}.

Table 1. Refined Structural Parameters by Using the Rietveld Method for NLNT_x Ceramics

<i>x</i>	space group	volume fraction	lattice parameters	<i>V</i> (Å ³)	<i>R</i> _{wp} (%)	<i>R</i> _p (%)	χ ²
0.05	<i>Pbma</i>	100%	<i>a</i> = 5.5564(1) Å, <i>b</i> = 15.5670(2) Å, <i>c</i> = 5.5028(1) Å, α = β = γ = 90°	475.970(6)	8.18	5.87	1.66
0.1	<i>Pbma</i>	100%	<i>a</i> = 5.5478(1) Å, <i>b</i> = 15.5823(2) Å, <i>c</i> = 5.5025(1) Å, α = β = γ = 90°	475.681(5)	8.17	6.34	1.53
0.15	<i>Pbma</i>	100%	<i>a</i> = 5.5398(1) Å, <i>b</i> = 15.5920(2) Å, <i>c</i> = 5.5018(1) Å, α = β = γ = 90°	475.226(5)	8.32	6.55	1.58
0.16	<i>Pbma</i>	15%	<i>a</i> = 5.5394(1) Å, <i>b</i> = 15.5894(2) Å, <i>c</i> = 5.5008(1) Å, α = β = γ = 90°	475.021(8)	9.68	7.43	1.79
	<i>Pnma</i>	85%	<i>a</i> = 7.7958(4) Å, <i>b</i> = 7.8030(4) Å, <i>c</i> = 23.4382(3) Å, α = β = γ = 90°	1425.745(24)			
0.18	<i>Pnma</i>	100%	<i>a</i> = 7.8104(2) Å, <i>b</i> = 7.7973(2) Å, <i>c</i> = 23.3985(6) Å, α = β = γ = 90°	1424.981(20)	9.23	6.95	1.74
0.2	<i>Pnma</i>	100%	<i>a</i> = 7.8053(3) Å, <i>b</i> = 7.7996(3) Å, <i>c</i> = 23.3982(8) Å, α = β = γ = 90°	1424.435(22)	9.85	7.80	1.62

II. EXPERIMENTAL PROCEDURES

The (Na_{1-x/2}La_{x/2})(Nb_{1-x}Ti_x)O₃ (NLNT_x, 0.05 ≤ *x* ≤ 0.2) solid-solution ceramics, BaCu(B₂O₅) (BCB), and the *x* = 0.18 ceramic doped with 1 mol % sintering aids (CuO, ZnF₂, and BCB) were prepared by a conventional solid-state reaction method. Nb₂O₅ (≥99.0%), Na₂CO₃ (≥99.0%), La₂O₃ (≥99.0%), TiO₂ (≥99.0%), ZnF₂ (≥99.0%), CuO (≥99.0%), Ba(OH)₂·8H₂O (≥99.0%), and H₃BO₃ (≥99.0%) powders were used as raw materials. The raw powders were weighed according to the chemical formula and dispersed by ball milling in ethanol with zirconia balls for 8 h. The mixed powders including NLNT_x and BCB were calcined at 850 and 810 °C for 4 h, respectively. Various sintering aids were added apart from calcined NLNT_{0.18} powder. The powders were remixed for 24 h and then pressed into disk samples with a diameter of 10 mm under 100 MPa. The sample disks of NLNT_x and the *x* = 0.18 samples with different sintering aids were sintered at 1285–1310 °C and 1050–1165 °C for 2 h, respectively. The ceramic disks were polished and coated with silver electrodes for testing electrical properties.

The crystal phases of the NLNT_x ceramics were determined using a powder X-ray diffractometer (XRD, D/Max-RB, Rigaku, Tokyo, Japan) with Cu Kα radiation. The density was estimated by the Archimedes method. Temperature- and frequency-dependent dielectric permittivity and impedance were measured using an LCR meter (Agilent E4980A, Santa Clara, CA). The *P*–*E* hysteresis loops were measured by using a ferroelectric testing system (Precision Multi-ferroelectric, Radiant Technologies Inc., Albuquerque, NM). The grain morphology was observed by field emission scanning electron microscopy (FE-SEM, SU8020, JEOL, Tokyo, Japan). Before the SEM observation, the samples were polished and then thermally etched at 1000 °C for 15 min. The *E*_B value was measured using a voltage breakdown tester (BDJC-50 kV, Beijing Beiguang Jingyi Instrument Equipment Co. Ltd., Beijing, China). The energy release properties were measured using a commercial charge–discharge platform (CFD-001, Gogo Instruments Technology, Shanghai, China). The samples with a thickness of 0.1 mm and an electrode diameter of 1.5 mm were used for electrical measurements, including *P*–*E* loops, dielectric breakdown, and the pulsed charge–discharge test. A field-emission transmission electron microscope (FE-TEM, JEM-2100F, JEOL, Japan) with a double-tilting stage was used to observe the domain morphology and high-resolution (HR) atomic image at 200 kV. Samples for the TEM examination were Ar-ion milled in a Precision Ion Polishing System (PIPS, Model 691, Gatan Inc., Pleasanton, CA, USA). Electric field-dependent Raman spectra were collected on the side surface of the pellets by 532 nm laser excitation using a Raman spectrometer (LabRam HR Evolution, HORIBA JOBIN YVON, Longjumeau Cedex, France), while external electric fields were applied simultaneously on two major sides of the samples perpendicular to the direction of the laser beam.

III. RESULTS AND DISCUSSION

Figure 2a shows the temperature- and frequency-dependent dielectric permittivity of NLNT_x ceramics. A sharp dielectric peak related to the *P*–*R* phase transition can be seen in the *x* = 0.05 sample at *T*_{*P*-*R*} ≈ 295 °C,^{18,19,37} which decreases sharply with further increasing *x*. A weak dielectric anomaly at about 150 °C as well as a significant improvement in room-

temperature dielectric permittivity can be seen simultaneously in the *x* = 0.16 ceramic, indicating that this composition at room temperature is dominated by a relaxor AFE *R* phase in addition to a tiny amount of residual AFE *P* phase. As *x* > 0.16, a single AFE *R* phase can be obtained at room temperature. An obvious dielectric relaxation behavior around the low-temperature phase transition peak can be observed for the AFE *R* phase compositions (for example, *x* = 0.18), as shown in the inset of Figure 2a. According to the previous study,²² this low-temperature dielectric peak at *T*_{*N*-*R*} should correspond to the transformation between the *FE* rhombohedral *N* phase and the AFE orthorhombic *R* phase. This low-temperature dielectric anomaly peak shifts toward lower temperature with further increasing *x*, thus leading a gradual decrease in room-temperature dielectric permittivity. The abovementioned phase transition process can be manifested by the Rietveld refinement results of the XRD patterns, as shown in Figure 2b and Table 1. The reliability factor of weighted patterns (*R*_{wp}), the reliability factor of patterns (*R*_p), and the goodness-of-fit indicator (χ²) are in the ranges of 8.17–9.85%, 5.87–7.80%, and 1.53–1.79, respectively, indicating that the agreement from the selected models is satisfactory.

The refinement results indicate that the complex substitution of A-site La³⁺ and B-site Ti⁴⁺ in NN can cause the disappearance of the AFE *P* phase and simultaneously stabilize the high-temperature AFE *R* phase at room temperature. From the local structure point of view, typical multiple-peak features in a range of 100–300 cm⁻¹ can be seen on the Raman spectra for 0.05 ≤ *x* < 0.16 samples in Figure 2c, which should be related to the unique structure of the AFE *P* phase with a complex octahedral tilting system and the large difference in B–O bond length.^{19,34} From locally enlarged Raman spectra in the inset of Figure 2c, an obvious shift to a lower wavenumber as well as a decreased peak intensity can be found for ν₄ and ν₅. The same feature can be also found for the ν₁ mode, indicating the decreased polarity of the basic perovskite unit cells, which is in favor of stabilizing the AFE *P* phase.^{21,22} Moreover, the split ν₄ modes become vague at *x* = 0.16 and then merge together as a shoulder when *x* ≥ 0.18 as a result of smaller difference between Nb–O bonds in the AFE *R* phase than AFE *P* phase.^{22,38}

The gradually weakened intensity, decreased wavenumber, and increased width in Raman peaks with increasing *x* in the AFE *R* phase zone suggest a gradually decreased polarity, a weakening bond between B-site cations and oxygen, and an increased structural disorder, respectively. These features should be compatible with the appearance of the macroscopic relaxor behavior, as observed in Figure 2a.

The *P*–*E* loops of NLNT_x ceramics during the second electric cycle were measured under their maximum testable electric fields, as shown in Figures 3a–c. A square-like hysteresis loop in the *x* = 0.05 ceramic suggests an irreversible

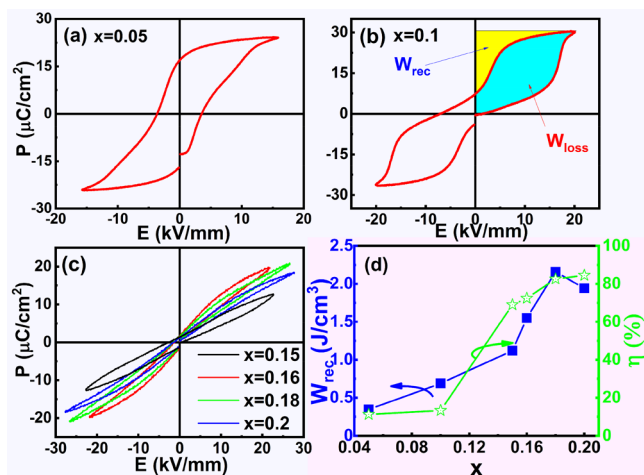


Figure 3. P - E loop of NLNT_x ceramics: (a) $x = 0.05$; (b) $x = 0.1$; and (c) $x = 0.15$, $x = 0.16$, $x = 0.18$, and $x = 0.2$. (d) W_{rec} and η values of NLNT_x ceramics as a function of x .

AFE-FE phase transition, leading to poor energy storage properties. An increase in the AFE P phase stability with increasing x is responsible for the typical repeatable double hysteresis loop at $x = 0.1$. However, unsatisfactory energy storage properties of $W_{\text{rec}} \approx 0.69 \text{ J/cm}^3$ and $\eta \approx 13\%$ can be obtained owing to the large polarization hysteresis and the low

E_{AF} value. Because of higher E_{AF} than the maximum testable electric field, a nearly linear hysteresis-free polarization response was obtained in the compositions of $x \geq 0.16$. Moreover, room-temperature dielectric permittivity rapidly increases with the entrance of the composition into the R phase zone (see Figure 2a). As a result, not only η but also W_{rec} can be simultaneously improved starting at $x = 0.16$, as shown in Figure 3d. A maximum $W_{\text{rec}} \approx 2.16 \text{ J/cm}^3$ as well as a relatively high $\eta \approx 82.6\%$ was obtained in the $x = 0.18$ ceramic.

Figure 4a presents the SEM images of $\text{NLNT}_{0.18}$ ceramics with and without 1 mol % sintering aids. It can be seen that all samples display a uniform and dense microstructure with a high relative density of $>97\%$. Clearly, the addition of sintering aids can significantly suppress the grain growth, yet the mechanisms are different for these additives. In the case of acceptor dopant CuO, the accumulation of formed oxygen vacancies at grain boundaries would hinder the grain growth during sintering, which might be responsible for a slight decrease in average grain size (G_a), as shown in Figure 4b.³⁹ However, the formation of defects would also activate the lattice, leading to a decrease in sintering temperature. By comparison, a drastic decline in average grain size was observed in ZnF_2 - and BCB-doped samples ($\sim 1.36 \mu\text{m}$ and $\sim 0.21 \mu\text{m}$, respectively), probably because of obviously reduced optimal sintering temperature from low-melting-point sintering aids. ZnF_2 has a low melting point of $\sim 872^\circ\text{C}$ and promotes sintering through particle rearrangement,

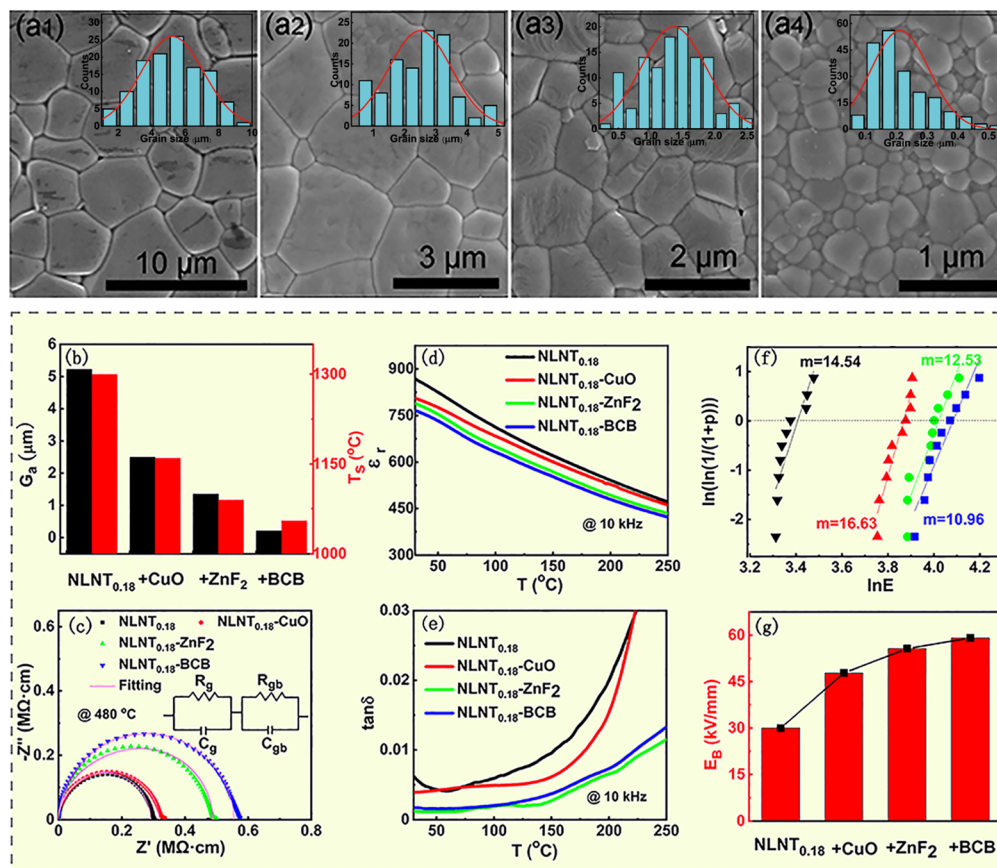


Figure 4. (a) SEM images of different ceramic samples ((a₁) $\text{NLNT}_{0.18}$, (a₂) $\text{NLNT}_{0.18}\text{-CuO}$, (a₃) $\text{NLNT}_{0.18}\text{-ZnF}_2$, and (a₄) $\text{NLNT}_{0.18}\text{-BCB}$) sintered at respective optimum sintering temperature (T_s) and the insets show the corresponding distribution of grain size. (b) G_a and T_s changing with different sintering aids. (c) Complex impedance data of different $\text{NLNT}_{0.18}$ samples. (d) Dielectric permittivity (ϵ_r) and (e) dielectric loss ($\tan\delta$) of different $\text{NLNT}_{0.18}$ samples. (f) Weibull distribution of the E_B and (g) determined E_B of the $x = 0.18$ samples with different sintering aids.

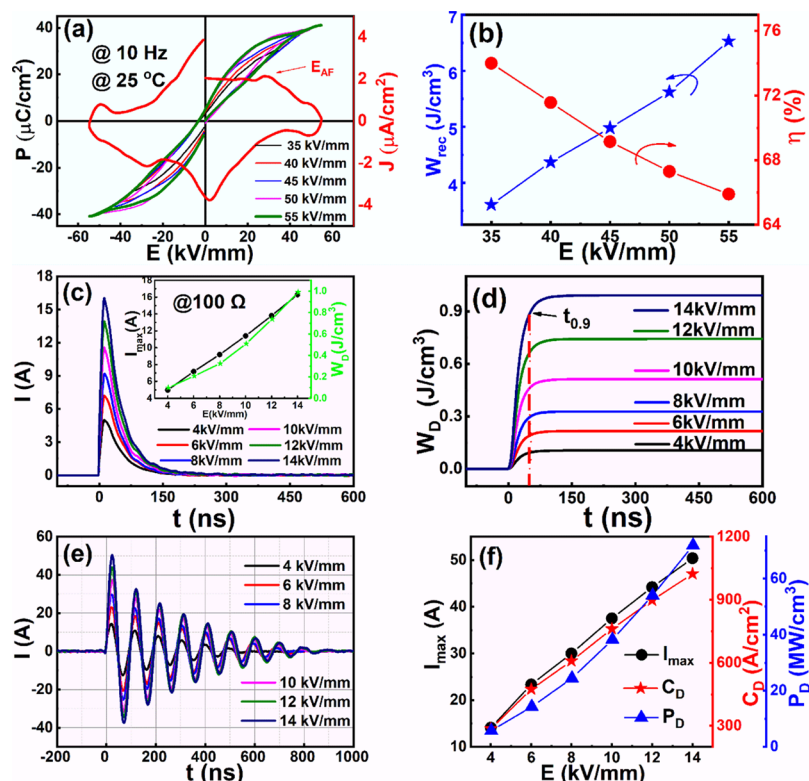


Figure 5. (a) P - E loops of the $\text{NLNT}_{0.18}\text{-0.01BCB}$ ceramic measured under different electric fields and the J - E curve under 55 kV/mm. (b) Evolution of W_{rec} and η values with applied electric field. (c) Electric field-dependent discharge current waveforms of $\text{NLNT}_{0.18}\text{-0.01BCB}$ in the overdamped circuit. (d) Relationship between W_{D} and time (t) of $\text{NLNT}_{0.18}\text{-0.01BCB}$ under different electric fields. (e) Electric field dependence of underdamped discharge waveforms of $\text{NLNT}_{0.18}\text{-0.01BCB}$ at room temperature. (f) I_{max} , C_{D} , and P_{D} as a function of electric field. The inset of (c) is the variation of I_{max} and W_{D} as a function of electric field.

dissolution-precipitation mass transfer, and a grain growth process. Differently, the phase of BCB tends to fill in the grain boundaries and prevents the grain growth but enhances densification through viscous flow at a relatively low temperature, as shown in Figure 4b. As a result, BCB-doped samples own even smaller grain sizes than ZnF_2 -doped samples. Moreover, a significant increase in total resistivity can be detected after doping. Particularly, the BCB-doped ceramic sample owns a total resistivity value twice as much as that of the undoped sample, as shown in Figure 4c. According to the fitting results by the equivalent circuit shown in the inset of Figure 4c, the conduction mechanism for the studied samples should be dominated by grain boundary. That is to say, the increased total resistivity after doping should be mainly related to the increased grain boundary fraction (i.e., reduced grain size).⁴⁰

At the same time, the improvement in sintering behavior after adding sintering aids accompanies a low dielectric loss of less than 0.5% as well as a slightly decreased dielectric permittivity, as shown in Figures 4d,e. The main conduction mechanism of ceramics is the movement of the charge carriers along the direction of electric field. The defects caused by adding acceptor CuO would tend to form stable defect dipoles with the oxygen vacancies, thus inhibiting long-range migration of oxygen vacancies. The obviously increased grain boundary fraction after adding ZnF_2 and BCB tends to increase the amount of depletion space charge layers. At the same time, the low-loss and high-resistivity BCB phase at grain boundaries would also decrease the possibility of electric breakdown. The

breakdown strength E_{B} can be estimated by the Weibull distribution⁴¹

$$X_i = \ln(E_i) \quad (1)$$

$$Y_i = \ln(\ln(1/(1 - P_i))) \quad (2)$$

$$P_i = i/(n + 1) \quad (3)$$

where E_i is the specific breakdown strength of each measured specimen, n is the sum of the measured samples, P_i is the breakdown probability, and i is the numerical order of the sample. As shown in Figure 4f, the main parameter representing the reliability of the statistical results is the Weibull modulus (m), which is the slope of the fitting line. The m value higher than 10 implies the credence of the statistic results. The average E_{B} value of each sample can be determined by using the intersection of the fitted curve with the horizontal axis, as given in Figure 4g. It is obvious that E_{B} values can be increased after adding sintering aids. According to the above analysis, this should benefit from the reduced grain size (Figure 4b), improved resistivity (Figure 4c), and declined dielectric loss (Figure 4e). Especially, the BCB-doped sample with submicron grains exhibits an ultrahigh EB ≈ 59 kV/mm, showing outstanding potential for improving energy storage properties.

To further disclose the energy storage performance of the $\text{NLNT}_{0.18}\text{-0.01BCB}$ ceramic, P - E loops were measured under different electric fields, as shown in Figure 5a, together with a polarization current versus electric field (J - E) curve under 55 kV/mm. A detectable polarization current peak can be

Table 2. Comparison of Energy Storage Properties among Various Reported Lead-Free Ceramics

composition	E (kV/mm)	W_{rec} (J/cm ³)	η (%)	G_a (μm)	phase	ref
Na _{0.7} Bi _{0.1} NbO ₃	25	3.44	85	6.75	RAF	25
0.93NaNbO ₃ -0.07Bi(Mg _{0.5} Zr _{0.5})O ₃	25.5	2.31	80.2	6.14	RAF	26
0.86NaNbO ₃ -0.14(Bi _{0.5} Na _{0.5})HfO ₃	35	3.51	80.1	1.68	RAF	27
AgNb _{0.85} Ta _{0.15} O ₃	23.3	4.2	69	~12	AFE	13
AgNbO ₃	17.5	2.1	-	~5	AFE	14
Sm _{0.03} Ag _{0.91} NbO ₃	29	5.2	68.5	2.12	AFE	15
0.9(K _{0.5} Na _{0.5})NbO ₃ -0.1Bi(Mg _{2/3} Nb _{1/3})O ₃	30	4.08	62.7	0.31	RFE	42
0.85BaTiO ₃ -0.15Bi(Mg _{0.5} Zr _{0.5})O ₃	30	2.9	86.8	3	RFE	3
BaTiO ₃ -Bi(Mg _{2/3} Nb _{1/3})O ₃ -0.3 wt % MnCO ₃	21	1.7	90	~2	RFE	29
0.8SrTiO ₃ -0.2(0.93Bi _{0.5} Na _{0.5} TiO ₃ -0.07Ba _{0.94} La _{0.04} Zr _{0.02} Ti _{0.98} O ₃)	32	2.83	85	1.72	RFE	6
0.61BiFeO ₃ -0.33BaTiO ₃ -0.06La(Mg _{0.5} Ti _{0.5})O ₃	13	1.66	82	2 ~ 3	RFE	28
0.65BiFeO ₃ -0.3BaTiO ₃ -0.05Bi(Zn _{2/3} Nb _{1/3})O ₃ -0.1 wt % Mn ₂ O ₃	18	2.1	53	~4	RFE	43
Bi _{0.5} K _{0.5} TiO ₃ -0.06La(Mg _{0.5} Ti _{0.5})O ₃	18	2.08	68	0.15	RFE	44
0.78(Bi _{0.5} Na _{0.5})TiO ₃ -0.22NaNbO ₃	39	7.02	85	0.5	RAF	5
0.6Bi _{0.51} Na _{0.47} TiO ₃ -0.4BaZr _{0.3} Ti _{0.7} O ₃	28	3.1	91	1.7	RFE	8
(Na _{0.25} Bi _{0.25} Sr _{0.5})(Ti _{0.8} Sn _{0.2})O ₃	31	3.4	89.5	2.7	RFE	7
NLNT _{0.18} -0.01BCB	55	6.5	65.9	0.21	RAF	this work

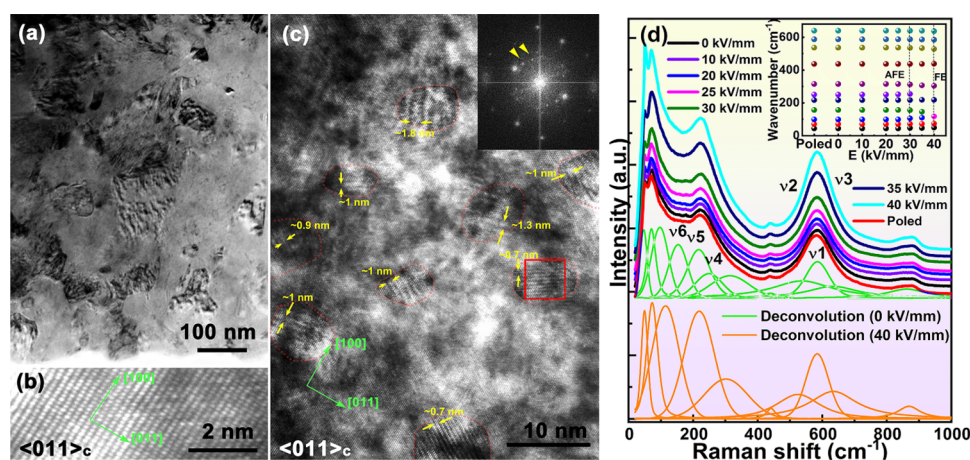


Figure 6. (a) TEM image and (b, c) HR-TEM images along the $\langle 110 \rangle_c$ direction for the BCB-doped NLNT_{0.18} ceramic. (d) Evolution of Raman spectra with changing external electric field and a representative spectral deconvolution into Gaussian-Lorentzian shape peaks for the NLNT_{0.18}-0.01BCB ceramic under electric fields of 0 and 40 kV/mm. The inset of (c) is the FFT of a selected nanosized pattern (the red square frame in Figure 6c) showing moiré fringes. The inset of (d) shows the variation of the wavenumber of Raman peaks with changing electric field.

observed in the J - E curve, which should originate from the AFE-FE phase transition approximately at 28 kV/mm, below which the current density remains almost unchanged. It can be seen that P_{max} monotonously increases but P_r remains nearly zero with increasing electric field. However, polarization hysteresis increases evidently with increasing electric field, probably because of the occurrence of the AFE-FE phase transition and reversible domain switching under higher electric fields. As a result, a monotonously increased W_{rec} as well as an obviously declined η can be obtained, as shown in Figure 5b. A giant W_{rec} of ~ 6.5 J/cm³ and a relatively high $\eta \approx 66\%$ were achieved under 55 kV/mm. In comparison with other (Na,M)(Nb,Ti)O₃ dielectric relaxor systems, NLNT_{0.18} shows a slightly smaller room-temperature ϵ_r value than (Na_{0.88}Bi_{0.12})(Nb_{0.76}Ti_{0.24})O₃ and (Na_{0.8}Sr_{0.2})(Nb_{0.8}Ti_{0.2})O₃ RAFs while a similar E_{AF} value to (Na_{0.88}Bi_{0.12})(Nb_{0.76}Ti_{0.24})O₃ and much higher than (Na_{0.8}Sr_{0.2})(Nb_{0.8}Ti_{0.2})O₃.^{22,24} Owing to the absence of the A-site lone pair effect, a smaller P_{max} was obtained in the NLNT_{0.18} ceramic than in (Na_{0.88}Bi_{0.12})(Nb_{0.76}Ti_{0.24})O₃, resulting in the decreased W_{rec} value. However, compared with other recently reported lead-free

ceramic materials, such as NN-, AgNbO₃-, (Na_{0.5}K_{0.5})NbO₃-, BaTiO₃-, SrTiO₃-, (Bi_{0.5}K_{0.5})TiO₃-, (Bi_{0.5}Na_{0.5})TiO₃-, and BiFeO₃-based compositions (see Table 2),^{3,5-8,13-15,25-29,42-44} the studied RAF sample in this work exhibits obvious advantages for future energy storage capacitors.

The pulsed charge-discharge measurements were used to evaluate the performance of pulsed capacitors in service. Figure 5c shows the room-temperature overdamped discharge current-time (I - t) waveforms of NLNT_{0.18}-0.01BCB under various electric fields, in which the current reaches its peak rapidly and then lasts for a very short time of ~ 200 ns. The peak current value increases monotonously with increasing applied electric field and reaches 16 A under 14 kV/mm, as clearly illustrated in the I_{max} - E curve (see the inset of Figure 5c). The corresponding discharged energy density (W_D) can be calculated using the following equation:

$$W_D = R \int I(t)^2 dt / V \quad (4)$$

where R of the total load resistor is 100 Ω and V is the sample volume. The discharged energy densities increase with

increasing applied electric field, which are ~ 0.103 and ~ 0.991 J/cm³ under 4 and 14 kV/mm, respectively. The discharge rate can be described by using the discharge time ($t_{0.9}$), which represents the time needed for releasing 90% of all stored energy. As shown in Figure 5d, a very short $t_{0.9}$ of ~ 50 ns can be found under the studied electric fields, indicating an ultrafast discharging speed for the studied ceramic. According to the electric field-dependent underdamped pulsed discharge curves shown in Figure 5e, it can be seen that I_{\max} , current density (C_D), and power density (P_D) values obviously increase with increasing electric field magnitude. Under 14 kV/mm, excellent properties such as $I_{\max} \approx 50.4$ A, $C_D \approx 1023$ A/cm², and $P_D \approx 71.8$ MW/cm³ can be obtained, as shown in Figure 5f. By comparing with other reported ceramics, the studied ceramic exhibits an ultrafast discharging speed.^{23,25,43–46} Together with the giant C_D and P_D values, the studied sample should have great potential in electrostatic energy storage and high-power systems.

The bright-field TEM image of the NLNT_{0.18}–0.01BCB ceramic is shown in Figure 6a. The dirty domain morphology corresponding to the AFE nanodomains can be observed. If one further looks into the HR-TEM image along the $\langle 110 \rangle$ direction (Figures 6b,c), periodic parallel stripes of ~ 1 nm in width can be seen, as marked in Figure 6c. Because the orientation of these stripes is random and deviates from both the $\langle 001 \rangle$ and $\langle 110 \rangle$ directions, these nanoregions might conform to the feature of moiré fringes, as can be further confirmed by the periodicity inside these patterns according to the superlattice diffraction dots in the fast Fourier transform (FFT) image in the inset of Figure 6c. The appearance of moiré fringes in AFEs/FEs is generally ascribed to the interference of two overlaid lattice patterns with mismatched orientations,⁴⁷ indicating the existence of short-range ordered dipoles in the sample. The size of antipolar nanoregions (APNRs)⁴⁸ in RAFs can be determined by the size of these mismatched regions, which is ~ 5 – 10 nm in radius. The size of APNRs found in the BCB-doped NLNT_{0.18} ceramic is slightly smaller than that in the (Na_{0.88}Bi_{0.12})(Nb_{0.76}Ti_{0.24})O₃ ceramic (30–50 nm), probably owing to ultrafine grains obtained in the studied sample.⁴⁹ The large random electric field, which is responsible for the disruption of long-range AFE ordering into APNRs, would increase the E_{AF} value through hindering the growth of APNRs into long-range ordered AFE domains.²⁴ This process can be further confirmed by in situ Raman results under different electric fields, as shown in Figure 6d. The Raman spectra remain almost unchanged till 25 kV/mm. With further enhancing electric field, a gradual increase in Raman intensity around ν_5 and ν_1 modes can be seen, apart from a gradual change in the peak shape, which can be clearly reflected on the deconvolution results in the inset of Figure 6d. The Raman modes at ~ 170 and ~ 250 cm⁻¹ (i.e., ν_6 and ν_4 vibrations, respectively)⁵⁰ gradually decrease in intensity above 30 kV/mm and disappear at 40 kV/mm, indicating the reconstruction of a long-range ordered FE phase.²² A good coincidence of the poled sample with the virgin sample in the Raman spectrum proves to be a reversible electric field-induced AFE–FE phase transition from the local structure point of view. As known, the APNRs exhibit zero macroscopic polarization under zero field, yet an FE state with large macroscopic polarization can be achieved under a strong external electric field. Owing to the highly polarizable APNRs as well as the existence of a large random field, the repeatable double-like P – E loop with a large E_{AF} of ~ 30 kV/mm and a

high P_{\max} value was achieved in the NLNT_{0.18}–0.01BCB RAF ceramic, providing the solid base for achieving excellent energy storage properties.

IV. CONCLUSIONS

The complex substitution of La³⁺ and Ti⁴⁺ in NN was found to not only effectively stabilize the high-temperature AFE R phase but also induce an obvious dielectric relaxor behavior, as evidenced by the Rietveld structural refinement of XRD patterns, frequency- and temperature-dependent permittivity vs temperature curves, Raman spectra, and P – E hysteresis loops. As a result, obviously enhanced energy storage properties can be obtained in the composition range of $x = 0.16$ – 0.20 for (Na_{1-x/2}La_{x/2})(Nb_{1-x}Ti_x)O₃ ceramics. In combination with the improvement in E_B values as a result of reduced grain size, enhanced resistivity, and declined dielectric loss after doping sintering aids, energy storage properties were further improved. Particularly, the BCB-doped $x = 0.18$ ceramic with submicron grains exhibits a giant $W_{\text{rec}} \approx 6.5$ J/cm³ and a large $\eta \approx 66\%$, $C_D \approx 1023$ A/cm², $P_D \approx 71.8$ MW/cm³, and $t_{0.9} \approx 50$ ns. The analysis of HR-TEM and in situ Raman spectra demonstrates the existence and rapid field-polarization response of APNRs as well as the resulting high E_{AF} value up to 30 kV/mm, providing a good understanding of the achievement of excellent energy storage properties in this work.

■ AUTHOR INFORMATION

Corresponding Author

Ruzhong Zuo – Institute of Electro Ceramics & Devices, School of Materials Science and Engineering, Hefei University of Technology, Hefei 230009, P.R. China;  orcid.org/0000-0001-8295-4323; Email: piezolat@hfut.edu.cn

Authors

Jun Chen – Institute of Electro Ceramics & Devices, School of Materials Science and Engineering, Hefei University of Technology, Hefei 230009, P.R. China

He Qi – Institute of Electro Ceramics & Devices, School of Materials Science and Engineering, Hefei University of Technology, Hefei 230009, P.R. China;  orcid.org/0000-0002-3094-3574

Complete contact information is available at:
<https://pubs.acs.org/10.1021/acsami.0c09876>

Notes

The authors declare no competing financial interest.

■ ACKNOWLEDGMENTS

This work was financially supported by the National Natural Science Foundation of China (grant nos. U19A2087 and U1432113).

■ REFERENCES

- (1) Chauhan, A.; Patel, S.; Vaish, R.; Bowen, C. R. Anti-Ferroelectric Ceramics for High Energy Density Capacitors. *Materials* **2015**, *8*, 8009–8031.
- (2) Yang, L.; Kong, X.; Li, F.; Hao, H.; Cheng, Z.; Liu, H.; Li, J.-F.; Zhang, S. Perovskite Lead-Free Dielectrics for Energy Storage Applications. *Prog. Mater. Sci.* **2019**, *102*, 72–108.
- (3) Yuan, Q.; Li, G.; Yao, F.-Z.; Cheng, S.-D.; Wang, Y.; Ma, R.; Mi, S.-B.; Gu, M.; Wang, K.; Li, J.-F.; Wang, H. Simultaneously Achieved Temperature-Insensitive High Energy Density and Efficiency in

Domain Engineered BaTiO₃-Bi(Mg_{0.5}Zr_{0.5})O₃ Lead-Free Relaxor Ferroelectrics. *Nano Energy* **2018**, *52*, 203–210.

(4) Yang, Z.; Gao, F.; Du, H.; Jin, L.; Yan, L.; Hu, Q.; Yu, Y.; Qu, S.; Wei, X.; Xu, Z.; Wang, Y.-J. Grain Size Engineered Lead-Free Ceramics with Both Large Energy Storage Density and Ultrahigh Mechanical Properties. *Nano Energy* **2019**, *58*, 768–777.

(5) Qi, H.; Zuo, R. Linear-Like Lead-Free Relaxor Antiferroelectric (Bi_{0.5}Na_{0.5})TiO₃-NaNbO₃ with Giant Energy-Storage Density/Efficiency and Super Stability Against Temperature and Frequency. *J. Mater. Chem. A* **2019**, *7*, 3971–3978.

(6) Yang, H.; Yan, F.; Lin, Y.; Wang, T. Novel Strontium Titanate-Based Lead-Free Ceramics for High-Energy Storage Applications. *ACS Sustainable Chem. Eng.* **2017**, *5*, 10215–10222.

(7) Yang, L.; Kong, X.; Cheng, Z.; Zhang, S. Ultra-High Energy Storage Performance with Mitigated Polarization Saturation in Lead-Free Relaxors. *J. Mater. Chem. A* **2019**, *7*, 8573–8580.

(8) Huang, Y.; Li, F.; Hao, H.; Xia, F.; Liu, H.; Zhang, S. (Bi_{0.51}Na_{0.47})TiO₃ Based Lead Free Ceramics with High Energy Density and Efficiency. *J. Materiomics* **2019**, *5*, 385–393.

(9) Li, W.-B.; Zhou, D.; Xu, R.; Wang, D.-W.; Su, J.-Z.; Pang, L.-X.; Liu, W.-F.; Chen, G.-H. BaTiO₃-Based Multilayers with Outstanding Energy Storage Performance for High Temperature Capacitor Applications. *ACS Appl. Energy Mater.* **2019**, *2*, 5499–5506.

(10) Zhang, L.; Jiang, S.; Fan, B.; Zhang, G. Enhanced Energy Storage Performance in (Pb_{0.858}Ba_{0.1}La_{0.02}Y_{0.008})(Zr_{0.65}Sn_{0.3}Ti_{0.05})O₃-(Pb_{0.97}La_{0.02})(Zr_{0.9}Sn_{0.05}Ti_{0.05})O₃ Anti-Ferroelectric Composite Ceramics by Spark Plasma Sintering. *J. Alloys Compd.* **2015**, *622*, 162–165.

(11) Gao, P.; Liu, Z.; Zhang, N.; Wu, H.; Bokov, A. A.; Ren, W.; Ye, Z.-G. New Antiferroelectric Perovskite System with Ultrahigh Energy-Storage Performance at Low Electric Field. *Chem. Mater.* **2019**, *31*, 979–990.

(12) Liu, Z.; Chen, X.; Peng, W.; Xu, C.; Dong, X.; Cao, F.; Wang, G. Temperature-Dependent Stability of Energy Storage Properties of Pb_{0.97}La_{0.02}(Zr_{0.58}Sn_{0.335}Ti_{0.085})O₃ Antiferroelectric Ceramics for Pulse Power Capacitors. *Appl. Phys. Lett.* **2015**, *106*, 262901.

(13) Zhao, L.; Liu, Q.; Gao, J.; Zhang, S.; Li, J.-F. Lead-Free Antiferroelectric Silver Niobate Tantalate with High Energy Storage Performance. *Adv. Mater.* **2017**, *29*, 1701824.

(14) Tian, Y.; Jin, L.; Zhang, H.; Xu, Z.; Wei, X.; Politova, E. D.; Stefanovich, S. Y.; Tarakina, N. V.; Abrahams, I.; Yan, H. High Energy Density in Silver Niobate Ceramics. *J. Mater. Chem. A* **2016**, *4*, 17279–17287.

(15) Luo, N.; Han, K.; Zhuo, F.; Xu, C.; Zhang, G.; Liu, L.; Chen, X.; Hu, C.; Zhou, H.; Wei, Y. Aliovalent A-Site Engineered AgNbO₃ Lead-Free Antiferroelectric Ceramics toward Superior Energy Storage Density. *J. Mater. Chem. A* **2019**, *7*, 14118–14128.

(16) Gao, F.; Dong, X.; Mao, C.; Liu, W.; Zhang, H.; Yang, L.; Cao, F.; Wang, G. Energy-Storage Properties of 0.89Bi_{0.5}Na_{0.5}TiO₃-0.06BaTiO₃-0.05K_{0.5}Na_{0.5}NbO₃ Lead-Free Anti-Ferroelectric Ceramics. *J. Am. Ceram. Soc.* **2011**, *94*, 4382–4386.

(17) Zhang, L.; Pu, Y.; Chen, M.; Liu, G. Antiferroelectric-Like Properties in MgO-Modified 0.775Na_{0.5}Bi_{0.5}TiO₃-0.225BaSnO₃ Ceramics for High Power Energy Storage. *J. Eur. Ceram. Soc.* **2018**, *38*, 5388–5395.

(18) Mishra, S. K.; Choudhury, N.; Chaplot, S. L.; Krishna, P. S. R.; Mittal, R. Competing Antiferroelectric and Ferroelectric Interactions in NaNbO₃: Neutron Diffraction and Theoretical Studies. *Phys. Rev. B* **2007**, *76*, No. 024110.

(19) Yuzyuk, Y. I.; Simon, P.; Gagarina, E.; Hennet, L.; Thiaudière, D.; Torgashev, V. I.; Raevskaya, S. I.; Raevskii, I. P.; Reznitchenko, L. A.; Sauvajol, J. L. Modulated Phases in NaNbO₃: Raman Scattering, Synchrotron X-ray Diffraction, and Dielectric Investigations. *J. Phys.: Condens. Matter* **2005**, *17*, 4977–4990.

(20) Shimizu, H.; Guo, H.; Reyes-Lillo, S. E.; Mizuno, Y.; Rabe, K. M.; Randall, C. A. Lead-Free Antiferroelectric: xCaZrO₃-(1-x)-NaNbO₃ System (0 ≤ x ≤ 0.10). *Dalton Trans.* **2015**, *44*, 10763–10772.

(21) Liu, Z.; Lu, J.; Mao, Y.; Ren, P.; Fan, H. Energy Storage Properties of NaNbO₃-CaZrO₃ Ceramics with Coexistence of

Ferroelectric and Antiferroelectric Phases. *J. Eur. Ceram. Soc.* **2018**, *38*, 4939–4945.

(22) Xie, A.; Qi, H.; Zuo, R.; Tian, A.; Chen, J.; Zhang, S. An Environmentally-Benign NaNbO₃ Based Perovskite Antiferroelectric Alternative to Traditional Lead-Based Counterparts. *J. Mater. Chem. C* **2019**, *7*, 15153–15161.

(23) Ye, J.; Wang, G.; Zhou, M.; Liu, N.; Chen, X.; Li, S.; Cao, F.; Dong, X. Excellent Comprehensive Energy Storage Properties in Novel Lead-Free NaNbO₃-Based Ceramics for Dielectric Capacitor Applications. *J. Mater. Chem. C* **2019**, *7*, 5639–5645.

(24) Qi, H.; Zuo, R.; Xie, A.; Tian, A.; Fu, J.; Zhang, Y.; Zhang, S. Ultrahigh Energy-Storage Density in NaNbO₃-Based Lead-Free Relaxor Antiferroelectric Ceramics with Nanoscale Domains. *Adv. Funct. Mater.* **2019**, *29*, 1903877.

(25) Zhou, M.; Liang, R.; Zhou, Z.; Dong, X. Superior Energy Storage Properties and Excellent Stability of Novel NaNbO₃-Based Lead-Free Ceramics with A-Site Vacancy obtained via a Bi₂O₃ Substitution Strategy. *J. Mater. Chem. A* **2018**, *6*, 17896–17904.

(26) Qu, N.; Du, H.; Hao, X. A New Strategy to Realize High Comprehensive Energy Storage Properties in Lead-Free Bulk Ceramics. *J. Mater. Chem. C* **2019**, *7*, 7993–8002.

(27) Yang, Z.; Du, H.; Jin, L.; Hu, Q.; Wang, H.; Li, Y.; Wang, J.; Gao, F.; Qu, S. Realizing High Comprehensive Energy Storage Performance in Lead-Free Bulk Ceramics via Designing an Unmatched Temperature Range. *J. Mater. Chem. A* **2019**, *7*, 27256–27266.

(28) Zheng, D.; Zuo, R. Enhanced Energy Storage Properties in La(Mg_{1/2}Ti_{1/2})O₃-Modified BiFeO₃-BaTiO₃ Lead-Free Relaxor Ferroelectric Ceramics within a Wide Temperature Range. *J. Eur. Ceram. Soc.* **2017**, *37*, 413–418.

(29) Li, W.-B.; Zhou, D.; Pang, L.-X. Enhanced Energy Storage Density by Inducing Defect Dipoles in Lead Free Relaxor Ferroelectric BaTiO₃-Based Ceramics. *Appl. Phys. Lett.* **2017**, *110*, 132902.

(30) Zhao, P.; Wang, H.; Wu, L.; Chen, L.; Cai, Z.; Li, L.; Wang, X. High-Performance Relaxor Ferroelectric Materials for Energy Storage Applications. *Adv. Energy Mater.* **2019**, *9*, 1803048.

(31) Zeng, J. T.; Kwok, K. W.; Chan, H. L. W. Ferroelectric and Piezoelectric Properties of Na_{1-x}Ba_xNb_{1-x}Ti_xO₃ Ceramics. *J. Am. Ceram. Soc.* **2006**, *0*, 2828–2832.

(32) Tripathi, S.; Lalla, N. P.; Pandey, D. Transmission Electron Microscopic Study of the Long Period Modulated Phase in the Morphotropic Phase-Boundary Region of (1-x)NaNbO₃-xCaTiO₃ for x=0.16. *Appl. Phys. Lett.* **2008**, *93*, 232903.

(33) Tripathi, S.; Pandey, D.; Mishra, S. K.; Krishna, P. S. R. Morphotropic Phase-Boundary-Like Characteristic in a Lead-Free and Non-Ferroelectric (1-x)NaNbO₃-xCaTiO₃ System. *Phys. Rev. B* **2008**, *77*, No. 052104.

(34) Sakowski-Cowley, A. C.; Łukaszewicz, K.; Megaw, H. D. The Structure of Sodium Niobate at Room Temperature, and the Problem of Reliability in Pseudosymmetric Structures. *Acta Crystallogr., Sect. B: Struct. Sci., Cryst. Eng. Mater.* **1969**, *25*, 851–865.

(35) Allred, A. L. Electronegativity Values from Thermochemical Data. *J. Inorg. Nucl. Chem.* **1961**, *17*, 215–221.

(36) Garg, R.; Senyshyn, A.; Boysen, H.; Ranjan, R. Structure and Phase Transition of Na_{0.5}La_{0.5}TiO₃. *J. Phys.: Condens. Matter* **2008**, *20*, S05215.

(37) Koruza, J.; Tellier, J.; Malič, B.; Bobnar, V.; Kosec, M. Phase Transitions of Sodium Niobate Powder and Ceramics, Prepared by Solid State Synthesis. *J. Appl. Phys.* **2010**, *108*, 113509.

(38) Lefkowitz, I.; Łukaszewicz, K.; Megaw, H. D. The High-Temperature Phases of Sodium Niobate and the Nature of Transitions in Pseudosymmetric Structures. *Acta Crystallogr.* **1966**, *20*, 670–683.

(39) Rahaman, M. N.; Manalert, R. Grain Boundary Mobility of BaTiO₃ Doped with Aliovalent Cations. *J. Eur. Ceram. Soc.* **1998**, *18*, 1063–1071.

(40) Irvine, J. T. S.; Sinclair, D. C.; West, A. R. Electroceramics: Characterization by Impedance Spectroscopy. *Adv. Mater.* **1990**, *2*, 132–138.

(41) Weihull, W. A Statistical Distribution Function of Wide Applicability. *J. Appl. Mech.* **1951**, *18*, 293–297.

(42) Shao, T.; Du, H.; Ma, H.; Qu, S.; Wang, J.; Wang, J.; Wei, X.; Xu, Z. Potassium-Sodium Niobate Based Lead-Free Ceramics: Novel Electrical Energy Storage Materials. *J. Mater. Chem. A* **2017**, *5*, 554–563.

(43) Wang, D.; Fan, Z.; Li, W.; Zhou, D.; Feteira, A.; Wang, G.; Murakami, S.; Sun, S.; Zhao, Q.; Tan, X.; Reaney, I. M. High Energy Storage Density and Large Strain in Bi(Zn_{2/3}Nb_{1/3})O₃-Doped BiFeO₃-BaTiO₃ Ceramics. *ACS Appl. Energy Mater.* **2018**, *1*, 4403–4412.

(44) Li, F.; Jiang, T.; Zhai, J.; Shen, B.; Zeng, H. Exploring Novel Bismuth-Based Materials for Energy Storage Applications. *J. Mater. Chem. C* **2018**, *6*, 7976–7981.

(45) Lin, Y.; Li, D.; Zhang, M.; Yang, H. (Na_{0.5}Bi_{0.5})_{0.7}Sr_{0.3}TiO₃ Modified by Bi(Mg_{2/3}Nb_{1/3})O₃ Ceramics with High Energy-Storage Properties and an Ultrafast Discharge Rate. *J. Mater. Chem. C* **2020**, *8*, 2258–2264.

(46) Li, W.-B.; Zhou, D.; Pang, L.-X.; Xu, R.; Guo, H.-H. Novel Barium Titanate Based Capacitors with High Energy Density and Fast Discharge Performance. *J. Mater. Chem. A* **2017**, *5*, 19607–19612.

(47) Liu, Q.; Zhang, Y.; Gao, J.; Zhou, Z.; Wang, H.; Wang, K.; Zhang, X.; Li, L.; Li, J.-F. High-Performance Lead-Free Piezoelectrics with Local Structural Heterogeneity. *Energy Environ. Sci.* **2018**, *11*, 3531–3539.

(48) Qi, H.; Zuo, R. Giant Electrostrictive Strain in (Bi_{0.5}Na_{0.5})-TiO₃-NaNbO₃ Lead-Free Relaxor Antiferroelectrics Featuring Temperature and Frequency Stability. *J. Mater. Chem. A* **2020**, *8*, 2369–2375.

(49) Cao, W.; Randall, C. A. Grain Size and Domain Size Relations in Bulk Ceramic Ferroelectric Materials. *J. Phys. Chem. Solids* **1996**, *57*, 1499–1505.

(50) Kakimoto, K.-i.; Akao, K.; Guo, Y.; Ohsato, H. Raman Scattering Study of Piezoelectric (Na_{0.5}K_{0.5})NbO₃-LiNbO₃ Ceramics. *Jpn. J. Appl. Phys.* **2005**, *44*, 7064–7067.